Inventory of Supporting Information

Manuscript #: 24020107A

Corresponding author name(s): Cedric Pilorget

Editorial Summary:

Hydrated Ammonium Magnesium-Phosphorus-rich ('HAMP') grains have been discovered in Ryugu samples. Embedded within an organic-rich phyllosilicate matrix, they may have been a key source of phosphorus and nitrogen in early terrestrial water reservoirs.

Peer Review Information:

Nature Astronomy thanks Matthew Pasek and the other, anonymous, reviewer(s) for their contribution to the peer review of this work.

1. Extended Data

Figure or Table #	Figure/Table title	Filename	Figure/Table Legend
Please group Extended Data items by type, in sequential order. Total number of items (Figs. + Tables) must not exceed 10.	One sentence only	Whole original file name including extension. i.e.: Smith_ED_Fig1.jpg	If you are citing a reference for the first time in these legends, please include all new references in the main text Methods References section, and carry on the numbering from the main References section of the paper. If your paper does not have a Methods section, include all new references at the end of the main Reference list.

Extended Data Fig. 1	IR spectral properties of A0218 extracted grain	Extended_data_Fig_1.tif	(left) Visible image of the grain extracted from A0218 aggregate sample obtained with the visible camera on the Agilent Cary 670/620 imaging microscope at SOLEIL Synchrotron facility. (right) MIR reflectance spectra of regions A (phosphate-rich) and B (matrix-rich) shown on the left image. A factor of x2 is applied to spectrum A.
Extended Data Fig. 2	SEM/EDS analyses of C0209 extracted particle	Extended_data_Fig_2.tif	Top. SEM analyses of C0209 extracted particle. Dots indicate the location of EDS analyses. P/Si atomic ratio highlight the P-rich areas. Bottom. Examples of EDS data obtained C0209 extracted particle. Point #6 shows a P, O and Mg-rich composition (characteristic of HAMP material), while Point #4 shows a typical Ryugu-matrix signature. The C peaks likely originate from the specific analytical protocol used, with grains placed on carbon nanotube tape (see Methods).
Extended Data Fig. 3	SEM/EDS analyses of A0218 extracted particle	Extended_data_Fig_3.tif	Top. SEM analyses of the A0218 extracted particle. Dots indicate the location of EDS analyses. P/Si atomic ratio highlight the P-rich areas. Bottom. Examples of EDS data obtained for the A0218 extracted particle. Point #14 shows a P, O and Mg-rich composition (characteristic of HAMP material), while Point #19 shows a typical Ryugu-matrix signature. The C peaks likely originate from the specific analytical protocol used, with grains placed on carbon nanotube tape (see Methods).
Extended Data Fig. 4	SXRD diffraction pattern obtained on a P-rich area of the	Extended_data_Fig_4.tif	Only small peaks from pyrrhotite, pentlandite and magnetite, typically present in matrix material that surrounds the P-rich areas, can be observed, suggesting the presence of matrix

	C0209 extracted particle		material on the P-rich areas. The absence of other features indicates that the P-rich material is mostly amorphous.
Extended Data Fig. 5	Correlation of 9.5 µm and 6.9 µm spectral features for C0209 extracted particle	Extended_data_Fig_5.eps	BD 9.5 µm vs. BD 6.9 µm from the data displayed in Figure 2, showing the correlation between both absorption features. Each point in the graph correspond to a 5x5 μm^2 pixel (thus no binning is applied). Pixels with a reflectance factor at 2.58 µm lower than 0.03 (corresponding to the absence of Ryugu material) have been removed, similar to Figure 2.
Extended Data Table. 1	Elemental abundances for C0209 and A0218 extracted particles	Extended_data_Tab_1.jpg	Elemental abundances, translated into modelled oxides, derived from SEM-EDS analyses on the C0209 and A0218 extracted particles (Sup. Fig. 2 and 3). Variability of Na_2O values (e.g., #21) also reflect µm-scale inhomogeneity in the Na content of the phyllosilicate-rich matrix [7].
Extended Data Table. 2	Atomic ratios for C0209 extracted particle	Extended_data_Tab_2.jpg	Atomic ratios derived from SEM-EDS analyses performed on the C0209 extracted grain (Sup. Fig. 2). The above table emphasizes the difference in composition of the HAMP (P-rich grains), point #6 in particular, with respect to the Si-rich matrix spots. Noticeably, the P-rich grains are Mg-rich, and almost Ca-free, which excludes apatite as a candidate.
Extended Data Table. 3	Atomic ratios for A0218 extracted particle	Extended_data_Tab_3.jpg	Atomic ratios derived from SEM-EDS analyses performed on the A0218 extracted grain (Sup. Fig. 3). The above table emphasizes the difference in composition of the HAMP (P-rich grains), points #11-15, with respect to the Si-rich matrix spots. Similar to C0209, the P-rich grains are Mg-rich, and almost Ca-free, which excludes apatite as a candidate.
Extended Data Table. 4	Solubility product constants and	Extended_data_Tab_4.jpg	

	solubilities (in mol/L) deduced at 298K.		
Extended Data Table. 5	Elemental abundances relative to Si in CI chondrite and Ryugu samples.	Extended_data_Tab_5.jpg	

Do not insert additional rows - total number of Extended Data items must not exceed 10.

1. Supplementary Information:

A. PDF Files

Item	Present?	Filename Whole original file name including extension. i.e.: Smith_SI.pdf. The extension must be .pdf	A brief, numerical description of file contents. i.e.: *Supplementary Figures 1-4, Supplementary Discussion, and Supplementary Tables 1-4.*
Supplementary Information	Choose an item.		
Reporting Summary	Choose an item.		
Peer Review Information	Choose an item.	*OFFICE USE ONLY*	

B. Additional Supplementary Files

Type	Number Each type of file (Table, Video, etc.) should be numbered from 1 onwards. Multiple files of the same type should be listed in sequence, i.e.: Supplementary Video 1, Supplementary Video 2, etc.	Filename Whole original file name including extension. i.e.: *Smith_ Supplementary_Video_1.mov*	Legend or Descriptive Caption Describe the contents of the file
Choose an item.			
Choose an item.			
Choose an item.			
Choose an item.			
Choose an item.			
Choose an item.			

Add rows as needed to accommodate the number of files.

3. Source Data

Parent Figure or Table	Filename Whole original file name including extension. i.e.: *Smith_SourceData_Fig1.xls,* or *Smith_ Unmodified_Gels_Fig1.pdf*	Data description i.e.: Unprocessed western Blots and/or gels, Statistical Source Data, etc.
Source Data Fig. 1	Figure_1_data_IR.xlsx	IR spectroscopic data
Source Data Fig. 2		

Source Data Fig. 3		
Source Data Fig. 4		
Source Data Fig. 5		
Source Data Fig. 6		
Source Data Fig. 7		
Source Data Fig. 8		
Source Data Extended Data Fig./Table 1	Extended_data_Fig_1_data_MIR_A0218.txt	IR spectroscopic data for A0218 extracted particle
Source Data Extended Data Fig./Table 2	Extended_data_Fig_2_EDS_spectra_WP_C0209.xlsx	EDS spectra of C0209 extracted particle
Source Data Extended Data Fig./Table 3	Extended_data_Fig_3_EDS_spectra_WP_A0218.xlsx	EDS spectra of A0218 extracted particle
Source Data Extended Data Fig./Table 4	Extended_data_Fig_4_ring-0000.tif-1031-70.csv	SXRD data of extracted particle
Source Data Extended Data Fig./Table 5		
Source Data Extended Data Fig./Table 6		
Source Data Extended Data Fig./Table 7		
Source Data Extended Data Fig./Table 8		

Source Data Extended Data Fig./Table 9		
Source Data Extended Data Fig./Table 10		

Title: Phosphorus-rich grains in Ryugu samples with major biochemical potential

Authors:

C. Pilorget[1,2], D. Baklouti[1], J.-P. Bibring[1], R. Brunetto[1], M. Ito[3,4], I. Franchi[5], N. Tomioka[3], M. Uesugi[6], A. Yamaguchi[7], R. Greenwood[5], T. Okada[8,9], T. Usui[8,9], T. Yada[8], K. Hatakeda[8,10], K. Yogata[8], D. Loizeau[1], T. Le Pivert-Jolivet[1], T. Jiang[1,11], J. Carter[1], V. Hamm[1], M. Abe[8,12], A. Aléon-Toppani[1], F. Borondics[13], Y. Enokido[8], Y. Hitomi[8,10], N. Imae[7], Y. Karouji[14], K. Kumagai[8,10], M. Kimura[7], Y. Langevin[1], C. Lantz[1], M.-C. Liu[15], M. Mahlke[1], A. Miyazaki[8], Z. Mughal[5], K. Nagashima[8], A. Nakano[8], A. Nakata[8], A. Nakato[7], M. Nishimura[8], T. Ohigashi[16], T. Ojima[8], F. Poulet[1], L. Riu[17], N. Shirai[18], Y. Sugiyama[8], R. Tahara[8], K. Uesugi[6], M. Yasutake[6], H. Yuzawa[19], A. Moussi-Soffys[20], S. Nakazawa[8], T. Saiki[8], F. Terui[21], M. Yoshikawa[8], S. Tanaka[8,12,22], S. Watanabe[23], Y. Tsuda[8,12]

Affiliations:

[1]Institut d'Astrophysique Spatiale, Université Paris-Saclay, CNRS, 91400 Orsay, France,
[2]Institut Universitaire de France, Paris, France
[3]Kochi Institute for Core Sample Research, JAMSTEC, Kochi 783-8502, Japan
[4]National Graduate Institute for Policy Studies (GRIPS)
[5]Open University, Walton Hall, Milton Keynes MK7 6AA, UK
[6]Japan Synchrotron Radiation Research Institute, SPring-8, Hyogo 679-5198 Japan
[7]National Institute of Polar Research, Tachikawa 190-8518, Japan
[8]Institute of Space and Astronautical Science, Japan Aerospace Exploration Agency, Sagamihara 252-5210, Japan,
[9]University of Tokyo, Bunkyo, Tokyo 113-0033, Japan,
[10]Marine Works Japan, Ltd, Yokosuka 237-0063, Japan,
[11]School of Earth Sciences, China University of Geosciences, Wuhan, China,
[12]The Graduate University for Advanced Studies (SOKENDAI), Hayama 240-0193, Japan,
[13]SMIS-SOLEIL, France
[14]Osaka University, Japan
[15]Lawrence Livermore National Laboratory, USA
[16]Photon Factory/Institute of Materials Science, High Energy Accelerator Research Organization
[17]European Space Agency (ESA), European Space Astronomy Centre (ESAC), Camino Bajo del Castillo s/n, 28692 Villanueva de la Canada, Madrid, Spain
[18]Kanagawa University, Japan
[19]Institute for Molecular Science, UVSOR Synchrotron Facility, Okazaki, Aichi 444-8585, Japan
[20]Centre National d'Etudes Spatiales, 18 Avenue E. Belin, 31401 Toulouse, France
[21]Kanagawa Institute of Technology, Atsugi 243-0292, Japan,
[22]University of Tokyo, Kashiwa 277-8561, Japan,
[23]Nagoya University, Nagoya, 464-8601, Japan.

Corresponding author:

Cedric Pilorget
email: cedric.pilorget@ias.u-psud.fr

Abstract:

Parent bodies of C-type asteroids may have brought key volatile and organic-rich compounds to the terrestrial planets in the early stages of the Solar System. At the end of 2020, the JAXA Hayabusa2 mission successfully returned samples from Ryugu, providing access to a primitive matter that has not suffered terrestrial alteration. We report here the discovery of a peculiar class of grains, up to a few hundreds of micrometres in size, that have a Hydrated Ammonium-Magnesium-Phosphorus-rich ('HAMP') composition. Their specific chemical and physical properties point towards an origin in the outer Solar System, beyond most snow lines, and their preservation along Ryugu history. Such phosphorus-rich grains, embedded within an organic-rich phyllosilicate matrix, may have played a major role when immersed in primitive terrestrial water reservoirs. In particular, in contrast to poorly soluble calcium-rich phosphates, HAMP grains favor the release of phosphorus-rich and nitrogen-rich ionic species, to enter chemical reactions. HAMP grains may have thus critically contributed to the reaction pathways of organic matter towards a biochemical evolution.

Main text:

On December 6, 2020, the Japanese Space Agency's (JAXA) Hayabusa2 mission successfully returned to Earth ~ 5.4 g of samples collected at the surface of the C-type asteroid Ryugu [1]. 'Chamber A' particles were collected on the natural surface of Ryugu, while 'chamber C' particles were collected close to an artificial crater so as to possibly access the sub-surface. These samples are stored and curated in an ultra-clean and controlled N_2-purged environment in the JAXA-ISAS (Institute of Space and Astronautical Science) Curation Facility and have thus remained unexposed to the terrestrial atmosphere since their collection. In this facility, a global non-destructive and non-invasive characterization of these samples is being performed. In particular, the MicrOmega near-infrared (NIR) hyperspectral microscope has identified inclusions and grains, some with sizes up to a few hundreds of micrometers of a variety of composition: organics, NH-rich and OH-rich phases, as well as minerals such as carbonates [2,3] all embedded within a dark matrix (near-IR reflectance factor of 2-3%) primarily made of phyllosilicates [1, 4-8]. In this paper, we focus on one class of grains/inclusions which uniquely exhibits a reflectance factor about 4-10 times higher than the matrix and a very peculiar broad and deep '3 µm' absorption feature (Figure 1a). This feature is attributed to O-H stretching vibrations of H_2O molecules (e.g., [9,10]). The position of this absorption band, beyond 3 µm, and its remarkably large width point toward particularly strong hydrogen bonds with different electronic environments (e.g., [11]). Noticeably, this feature which is not present in the matrix and other minerals, has been observed through the near-IR spectra acquired in the Curation Center, where the samples were always maintained in an H_2O-free environment since their collection. This observation implies that the H_2O molecules present in these high-reflectance grains are non-terrestrial. The spectra of these peculiar grains also display a sharp band at ~2.7 µm shifted by ~10 nm towards longer wavelengths compared to the feature exhibited by the phyllosilicates present in the matrix [2,12], as well as additional bands between 2.0 and 2.2 µm for the larger grains (Figure 1a).

Extended characterization after extraction

In order to refine their composition, two grains with such spectral properties were extracted from aggregate samples, one from C0209 (Figure 2) and the other from A0218 (Extended Data Figure 1) for complementary characterization. Combined analyses were then performed at the Kochi Institute for Core Sample Research of Japan Agency for Marine-Earth Science and Technology (JAMSTEC, Japan), Institut d'Astrophysique Spatiale (IAS, France) and Open University (OU, UK).

SEM-EDS (Scanning Electron Microscopy – Energy Dispersive Spectroscopy) analyses revealed an elemental composition primarily made of phosphorus, oxygen and magnesium (Figure 3, Extended Data Figure 2, 3 and Extended Data Tab. 1) with the atomic ratio P/Mg ~1, and almost no silicon (the prime constituent of the matrix silicates), nor calcium (Ca/Mg is below the percent level) (see Extended Data Tab. 2 point #6 and Extended Data Tab. 3 points #11,12 14). Some sodium also appears collocated with phosphorus in these grains (Figure 3), at a low abundance and highly variable level (Na/Mg < 1%, Extended Data Tab. 2 and 3). Additionally, this phosphorus-based compound appears poorly crystalline from XRD (X-Ray Diffraction) analyses, at least at the scale of a few tens of microns (Extended Data Figure 4). Further analysis by mid-IR micro-spectro-imagery (2.5-12 µm) has been carried out at the SOLEIL Synchrotron facility (SMIS beamline) to complement the MicrOmega NIR (0.99-3.6 µm) characterization performed within the Curation Center (Figure 1b, Figure 2 and Extended Data Figure 1). Noticeably, correlated features at 3 µm, 6.9 µm and a broader one centered around 9.5 µm have been observed on the P-O-Mg-rich areas (Extended Data Figure 5). The ~9.5 µm spectral feature is attributed to P-O stretching vibrations (e.g., [13,14]). The 6.9 µm band is attributed to the out-of-plane bending vibration (ν_4) in NH_4^+ (e.g., [15-17]). This identification is consistent with the presence in MicrOmega spectral data acquired in the Curation Center of a double peak feature at ~2.03 and ~2.15 µm (respectively attributed to NH_4^+ ν_2+ ν_3 and ν_3+ ν_4 combination modes [17,18]) for the larger grains, as well as small ~3.06-3.1 µm and ~3.25-3.3 µm features, respectively due to the asymmetric and symmetric stretching vibrations in NH_4^+ (e.g., [17,19,20]) observed in some cases within the broad 3 µm band.

Although each analytical method alone is insufficient to provide definite answers about what the analyzed grains are, the combination of near-IR/mid-IR spectroscopy and SEM/EDS elemental composition data offers a key diagnostic: Ryugu contains Hydrated Ammonium-Magnesium-Phosphorus-rich grains (referred to as HAMP grains) in which phosphorus is oxidized, plausibly as phosphate. In addition, these HAMP grains are most likely an ionic solid stabilized by the structural H_2O (e.g., [21]) thanks to strong hydrogen bonds with NH_4^+ and P-O-rich ions.

Discussion

While only a limited number of extracted grains were fully characterized outside the Curation facility, HAMP grains and inclusions are commonly present in Ryugu samples, as identified by the MicrOmega analyses. Several tens of areas with sizes up to a few hundred micrometers have been highlighted (examples on Figure 4). Inclusions at scales smaller than the MicrOmega spatial resolution (~20 µm) are also likely to exist as several detections are close to the detection limit.

The other ubiquitous P-O rich compound found in Ryugu samples is the Ca-phosphate apatite [5-7], also detected in carbonaceous chondrites (e.g., [22,23]). Minerals from the apatite group are poorly soluble (Extended Data Tab. 4). In the case of Ryugu samples, apatite was mostly observed in the form of hydroxyapatite ($Ca_5(PO_4)_3(OH)$). Additionally, the presence of phosphides (schreibersite $(Fe, Ni)_3P$ and allabogdanite $(Fe, Ni)_2P$) has been reported in the least altered fragments [6], as well as a few Mg-phosphate-rich areas, some with small amounts of Na [5-7, 24].

The formation of HAMP grains, by contrast to the other P-O rich ionic solid hydroxyapatite, puts strong constraints on the formation and evolution of Ryugu's parent body. The synthesis of HAMP requires that Ca^{2+} ions were highly depleted relatively to Mg^{2+} ions, while phosphorus, plausibly initially present in phosphide compounds, had already been oxidized. The scenario we propose to account for the favored formation of HAMP with respect to Ca-phosphates is determined by the larger availability of Mg^{2+} (and NH_4^+) ions compared to Ca^{2+}, as a result of the competing formation of Ca-rich carbonates.

The early availability of Ca^{2+} and CO_3^{2-}, the latter of which possibly originated from ices [6], would have favored the formation of Ca-rich carbonates [3]. The resulting huge depletion in Ca^{2+} relatively to Mg^{2+}, and an increasing availability of P-O-rich ions, led to the formation of HAMP. Such a scenario is supported by the detections of calcium carbonates, phosphides and 'Mg-Na phosphates' in the least altered fragments of Ryugu, while no hydroxyapatite was observed in those samples [6]. In a similar way, [25] reported the presence in Orgueil of Ca-carbonates in a clast that shows little alteration, with no detectable apatite content.

With some Ca^{2+} ions remobilized and some PO_4^{3-} ions still available or also remobilized, apatites would have formed, at least in some localized sites, as is observed in Ryugu samples. The formation of (Mg,Fe)-carbonates (such as breunnerite) would have occurred when Ca^{2+} ions were no longer available, after that of (Mg,Ca)-carbonates (such as dolomite) and apatites. Such a scenario would be consistent with the suggestion by [3] that dolomite formed within small pores present in the precursor material, while the formation of Fe-rich magnesite (breunnerite) occurred later in larger fractures.

The presence of ammonium cations NH_4^+ within the HAMP compounds supports the suggested scenario that Ryugu's parent body formed in the outer Solar System, beyond H_2O, NH_3 and CO_2 snow lines [3,4,6,26-28], in particular for requiring NH_4^+ ions, a major specie detected in extraterrestrial matter (e.g., [29,30]), likely trapped in ices. Similar to CO_3^{2-} ions, NH_4^+ can thus be readily available to enter reaction processes within the accreted Ryugu parent body, possibly at icy grain surfaces and form ionic solids such as HAMP grains. The same process could also account for the coupled inclusion of structural H_2O molecules responsible for the large 3 µm feature that was detected exclusively in these grains. Water molecules are indeed mostly absent from the matrix [31,32], in which the hydroxyl moiety (M-OH) is detected through the 2.7 µm absorption band (e.g., [12]). Some water molecules together with ammonium cations would thus have been trapped in HAMP inclusions and would constitute unique remnants from the primary ices.

The importance of the detection of HAMP grains/inclusions in Ryugu samples comes from their much higher solubility in liquid water with respect to apatites. Solubility is indeed directly related to the lattice energy of the different ionic solids at stake and to the hydration enthalpy of the different ions forming the compound. First, because of its smaller size, Mg^{2+} has a much lower hydration enthalpy than Ca^{2+} that makes it easily solvated. Then, apatite is by far the ionic structure with the strongest lattice energy among the different phosphates (and carbonates) identified. Such a parameter characterizes the stability of the ionic solids and, thus, their ability to be thermodynamically favored if the contributing ions are available, and reversely it will affect their solubility in liquid water. As a result, hydroxyapatite is the least soluble specie among the above-mentioned list of compounds (Extended Data Tab. 4). Comparatively, the solubility of struvite ($NH_4MgPO_4 . 6H_2O$), the best well characterized compositional analogue to HAMP compounds, is more than two orders of magnitude higher than that of hydroxyapatite in water at 298 K (Extended Data Tab. 4). In the competition between the formation of Ca-phosphates and Mg-phosphates, hydroxyapatite is thus strongly favored provided that Ca^{2+} and PO_4^{3-} ions are available.

As calcium is about 10 times more abundant than phosphorus in Ryugu samples (Extended Data Tab. 5), the formation of hydroxyapatite would have entirely consumed phosphorus while the calcium abundance would have remained almost unchanged. Since phosphorus is quite scarce (P/Si=0.0073±0.0001, Extended Data Tab. 5) and hydroxyapatite very stable and particularly poorly water-soluble, it is unlikely that a significant part of the phosphorus would have been remobilized in a later 'alteration' event to form the HAMP inclusions that have been detected, especially at the low temperatures experienced by Ryugu and its parent body (e.g., [6,31,33]). Therefore, as explained above, the formation of HAMP grains vs hydroxyapatite is primarily determined by the availability of constitutive ions (e.g., [34]). The presence of HAMP grains thus translates the competition between the formation of phosphates and that of carbonates, for their coupled role in integrating and thus

depleting both Ca and Mg ions (e.g., [35-38]). In particular, the local closed-system environments that may have been in place on such primitive bodies may have been key to limit the formation of apatites by depleting calcium in the environment through the formation of carbonates and to favor that of hydrated-ammonium-magnesium-phosphorus-rich grains.

The presence of HAMP grains, therefore, puts strong constraints on the sequence of formation of the different constituents and on the evolution of the environment of their parent body, since their earliest formation phases within the protoplanetary disk, possibly from a reservoir similar to that of some comets [30,39]. Although HAMP grains likely originated from the outer Solar System, their occurrence in Ryugu samples indicates that they remained preserved since their formation, as a key record of the sequence of events that the Ryugu parent bodies experienced, throughout their history. As quoted above, part of the stability of HAMP grains likely originates from the presence of H_2O molecules in their structure. Noticeably, the preservation of NH_4^+ ions indicates that HAMP have not suffered major thermal heating since their formation [40].

Finally, this discovery delivers a critical outcome of biochemical relevance, with respect to the role such grains may have played when they were brought to the inner Solar System together with CHNOS compounds (e.g., [4, 41-43]), and then immersed in the ancient terrestrial water reservoirs (e.g., [44]). By contrast to apatites, which tend to strongly limit the availability of phosphorus-rich compounds for further chemical reactions once formed (known as the 'phosphate problem' [45-46]), HAMP favors its release by dissolution in liquid water. These minerals would have also displayed a much greater reactivity than that of phosphates from the apatite group, in particular thanks to the presence of ammonium and of the Mg^{2+} divalent cation [47,48]. Moreover, the coupled delivery of soluble P-rich and reduced N-bearing phases through the HAMP grains, together with an organic-rich Ryugu-like matter, might have favored a rapid reaction chain against the water dilution. It is noticeable that the P/C ratio in Ryugu grains is close to that in biomass (Extended Data Tab. 5, [49,50]). They may have offered a pathway towards the formation of organophosphorus compounds, including organophosphates, known to be part of biomolecules such as RNA, DNA and ATP, and phosphorylation reactions (e.g., [48,51]). Actually, the ability of the struvite analogue to form organophosphates with good yields has been reported by various surveys (e.g., [34,51-54]). HAMP grains, coupled to the organics present in the same material, formed in the outer protoplanetary disk and preserved till their delivery to terrestrial standing water, would have been essential providers of phosphorous, carbonaceous and nitrogenous compounds to biochemical syntheses.

Methods:

MicrOmega:

The methodology regarding the MicrOmega instrument within the Curation Facility is similar to that presented in [2,3]. MicrOmega is mounted in an ultraclean-N_2 purged chamber to prevent H_2O/CO_2 contamination. The instrument is cooled down by being mounted on a copper plate maintained at 10°C to decrease thermal emission within the instrument and increase the signal-to-noise ratio (SNR). To be imaged by MicrOmega, the samples are introduced within a "Sample Chamber" part of the main Curation Facility suite [1] separated from the MicrOmega chamber by a NIR-transparent sapphire (Al_2O_3) window. The Sample Chamber, which has been extensively ultracleaned as the entire facility suite, is permanently flowed with N_2. Each sample is deposited on a dedicated sapphire sample holder set on a polished gold-coated mirror. The sample holder is set on a (x,y,z,θ) moving stage, remotely controlled, enabling to locate the entire surface of the sample within the MicrOmega Field of View (FoV) and to illuminate the grains with different azimuth angles. The MicrOmega instrument sequentially illuminates the sample at different wavelengths with an incidence angle of ~35°. For each illuminated wavelength, an image is acquired in a "nadir" configuration on a 2D Mercury-Cadmium-Telluride sensor, cooled down to 110K with a dedicated cryocooler. An hyperspectral (x,y,λ) cube is built by scanning the different monochromatic channels in the 0.99-3.65 µm wavelength range. Thanks to the use of an Acousto Optic Tunable Filter (AOTF) as dispersive system, with a Full Width at Half Maximum of ~20 cm^{-1}, the wavelengths can be selected and repeated in any order with minimum sampling steps of ~2 cm^{-1}. For the baselined operations, the typical number of spectral channels per cube varies between ~200 and ~400. Importantly, as the AOTF is electronically controlled, it offers the capability to measure and subtract "on-the-fly" the background signal, originating from the thermal emission of the sample, the thermal emission of the instrument, the straylight and the dark current, by successively switching ON and OFF the AOTF. This procedure, baselined for routine operations, makes the instrument insensitive to long-term temperature variations during the observation, and significantly enhances the retrieval of the scientific signal detected. Since the dispersive system is part of the illumination path, the thermal background (from both the sample and the instrument) measured by the instrument is integrated over the entire spectral range (and thus does not vary with the wavelength of the illuminating beam). The calibration process and the resulting performances are fully described in [55]. The radiometric calibration is evaluated to be better than 20% in absolute value, and ~1% in relative value (from one spectral channel to the next). The spectral accuracy is evaluated to be within ±2.5 nm.

First, bulk samples A1-A3 and C1-C3 [1] were analyzed by the suite of instruments installed within the ISAS Curation Facility, including MicrOmega. Then, aggregate samples and individual (mm-sized) grains were extracted from the initial bulk samples and analyzed in a similar way. Details about the different samples can be found at the JAXA Data Archives and Transmission System (DARTS) https://www.darts.isas.jaxa.jp/curation/hayabusa2/.

Particle extraction and SEM-EDS at the Kochi Institute for Core Sample Research:

White particles used in this study were extracted by the Phase 2 Curation team at the Kochi Institute for Core Sample Research, JAMSTEC. The C0209 (5.3 mg) and A0218 (13.1 mg) samples consist of aggregates with a particle size < 1 mm. The extraction of the white particle from C0209 was conducted under a pure nitrogen condition in a glove box but for A0218, it was carried out under the ambient atmospheric condition in a clean bench. The white particles from C0209 and A0218 were placed on a carbon nanotube tape (CNT). They were then subject to imaging and compositional analyses by

secondary electron and back-scatted electron microscopy, with a Hitachi High-Tech SU1510 SEM equipped with a Horiba Emax EDS detector. Noticeably, the EDS detector window prevents from detecting low X-ray energy atoms (e.g., N), except when at very large abundance, typically a few tens of wt% (e.g., [56] for N, C from CNT).

XRD:

A fraction of the white particle extracted from C0209 was examined by synchrotron X-ray diffraction (SXRD) at the beamline BL 20XU at SPring-8, Japan. X-ray diffraction patterns were acquired from bulk volume of the sample. The detector (BM AA60, Hamamatsu Photonics) is equipped with a scintillator consisting of a P43 (Gd_2O_2S: Tb) powder screen that is 50 µm thick, the complementary metal oxide semiconductor (CMOS) camera (which has 2304 × 2304 pixels (C15440-20UP, Hamamatsu Photonics)) and relay lenses. The pixel size of the detector is 19.05 µm and the field of view was 39x39 mm^2. An X-ray beam with 30 KeV of energy was focused by a Fresnel zone plate. The detector for the X-ray diffraction mode was placed 110 mm behind the sample, with a 3 mm beam stop just in front of the detector. Diffraction images from 2ϑ = 1.43° to 18.00° were obtained by the detector. Samples were vertically translated with a certain interval, and half-rotated for each vertical scan step. Diffraction of mineral grains in a horizontal plane can be obtained if the mineral grains meet the Bragg condition in the half rotation. Diffraction images were then integrated into one image for each vertical scan step.

Mid-IR micro-spectro-imagery:

The Mid-IR (MIR) reflectance analyses have been performed at the SOLEIL facility, France, with an Agilent Cary 670/620 imaging microscope using a Globar source and equipped with a 128x128 pixel focal plane array (FPA) detector sensitive in the spectral range from 2.5 to 12 µm (spectral resolution of 8 cm^{-1}). We used an x15 objective, which gives a pixel size of 5.5x5.5 μm^2 (FoV=704x704 μm^2). The radiometric calibration was performed using a reference gold mirror.

SEM-EDS on C0209 pressed particle:

A portion of the white particle mounted on the CNT was removed and pressed into a gold foil following methodology previously used for samples such as interplanetary dust particles (e.g., [57]). The sample was imaged (SE and BSE) on the Zeiss Crossbeam 550 SEM at the Open University. An EDS map was made of the white particle plus some of the surrounding matrix material. This approach only provides semi-quantitative results, although reproducibility was generally good for O, Mg and P (at few % level). The EDS detector window prevents from detecting low X-ray energy atoms (e.g., N), except when at very large abundance.

Data availability:

Images and source data are provided with this paper. IR spectral data obtained in the ISAS Curation Facility will also be available in the catalogue of Ryugu samples (https://www.darts.isas.jaxa.jp/curation/hayabusa2/). Other data and images on the Ryugu samples are available at the same address.

Code availability:

N/A

Acknowledgments:

We deeply thank the entire Hayabusa2 team for the opportunity to be part of this outstanding mission. We also thank the Centre National d'Etudes Spatiales (CNES) for its full support. The Mid-IR microspectroscopy measurements were supported by grants from Region Ile-de-France (DIM-ACAV) and SOLEIL. This research was also supported in part by the JSPS KAKENHI (grant numbers JP18K18795, JP18H04468 and JP23H01238 to M.Ito).
Finally, we would like to offer special thanks to B. Gondet, who, although no longer with us, contributed largely to this work.

Author contributions:

D.B., R.B., M.I., I.F., N.T., M.U., A.Y., R.G., T.O., T.U., T.Y., A.Nakato, V.H., J.-P.B., C.P., F.B. conceived and designed the experiments and the workflow.
D.L., C.P., R.B., T.Y., K.H., K.Y., T.L.P-J., L.R., Y.E., Y.H., K.K., C.L., M.M., A.M., K.N., A.Nakano, A.Nakata, M.N., T.Ojima., L.R., Y.S. and R.T. performed the measurements with MicrOmega.
M.O. conducted the sample handling in the glovebox after extraction from the ISAS Curation Facility.
M.I. and N.T. performed the SEM/EDS measurements.
M.U., A.Y., N.I., N.T. and M.I. performed the SXRD measurements.
D.B., R.B. and C.P. performed the mid-IR micro-spectro-imagery measurements at Soleil Synchrotron.
I.F., R.G. and Z.M. prepared the C0209 white particle extract pressed into a gold foil and performed the SEM-EDS measurements.
C.P., D.B., J.-P.B., R.B, M.I., I.F., N.T., M.U., A.Y., R.G., D.L., T.L.P-J., T.J., J.C., V.H., Y.L., F.P. and L.R. contributed to the data processing, analysis and interpretation.
C.P., D.B., J.-P.B. and R.B. wrote the draft of the manuscript.
All co-authors were involved in the discussions of the results and the finalization of the manuscript.

Competing interests:

The authors declare no competing interests.

Figure captions:

Figure 1: IR spectral characterization.

(a) NIR reflectance spectra obtained by MicrOmega in the Curation Center on HAMP-rich areas shown in Figure 4. Vertical lines are set at 2.03, 2.15, 2.725, 3.06 and 3.28 µm.
(b) Mid-IR reflectance spectra by the micro-spectro-imager of regions S1 (HAMP-rich) and S2 (matrix-rich) shown in Figure 2C. Blue arrows respectively point towards N-H (at 6.9 µm) and P-O (at ~9.5 µm) features. Green arrows point towards (H-)O-H features at ~3 µm and ~6 µm due to endogenous water and possibly water from terrestrial contamination since the samples were exposed to the terrestrial atmosphere for MIR spectroscopic analyses. Dotted lines show the Christiansen feature for both S1 (in black) and S2 (in gray) spectra. The P-O feature at ~9.5 µm is present as a peak since it is the surface scattering regime at wavelengths > 8 µm, and is distinct from the Si-O feature at ~10 µm that can be observed on areas where matrix material is present.

Figure 2: C0209 extracted particle

(A) Visible image of the grain extracted from C0209 aggregate sample obtained with an optical microscope; (B) Reflectance map at 2.58 µm; (C) same as (B) with the location of spectra displayed on Figure 1; (D) 3.0 µm relative band depth map; (E) 6.9 µm relative band depth map; (F) 9.5 µm relative band depth map. These maps are based on spectral features shown in Figure 1b. Pixels with a reflectance factor at 2.58 µm lower than 0.03 (corresponding to the absence of Ryugu material) have been removed from panels D, E and F.

Figure 3: Elemental analysis.

EDS maps of a fraction of the particle extracted from C0209 ("white part" observed in Figure 2A), pressed on a gold foil and observed in SEM (left). EDS data indicate that P-rich areas are Si-free, and conversely: Si is a major constituent of the matrix, and is not detected in the P-rich grains. Importantly, the P-rich area includes Mg but no Ca, excluding apatite.

Figure 4: Examples of HAMP grains

False-color RGB maps (R: 3.2 µm, G: 2.8 µm, B: 2.5 µm, square-root stretch) of selected regions in which grains/inclusions with spectral signatures similar to the extracted particle are observed. The HAMP-rich areas display a blue color and are indicated by white arrows. Observations were performed in the Curation Center on bulk 'A3' (3rd bulk sample from chamber A) (A) 'aggregate' samples C0209 (B) and C0107 (C) and grain A0001 (D). Averaged spectra of the HAMP-rich areas are shown in Figure 1a. Artefacts due to shadowing can be observed on the edges of the grain on panel (D).

References :

[1] Yada, T. et al. Preliminary analysis of the Hayabusa2 samples returned from C-type asteroid Ryugu. *Nat. Astron.* 6, 214-220 (2022)
[2] Pilorget, C. et al. First compositional analysis of Ryugu samples by the MicrOmega hyperspectral microscope. Nat. Astron. 6, 221-225 (2022)
[3] Loizeau, D. et al. Constraints on Solar System early evolution by MicrOmega analysis of Ryugu carbonates. *Nat. Astron.* 7, 391-397 (2023)
[4] Ito, M. et al. A pristine record of outer Solar System materials from asteroid Ryugu's return sample. *Nat. Astron.* 6, 1163-1171 (2022)

[5] Nakamura, E. et al. On the origin and evolution of the asteroid Ryugu: A comprehensive geochemical perspective *Proc. Jpn. Acad.* Ser. B 98 227-282 (2022)
[6] Nakamura, T. et al. Formation and evolution of carbonaceous asteroid Ryugu: Direct evidence from returned samples. *Science* 379, Issue 6634, article id. abn8671 (2023)
[7] Yamaguchi, A. et al. Insight into multi-step geological evolution of C-type asteroids from Ryugu particles*. Nat. Astron.* 7, 398-405 (2023)
[8] Tomioka, N. et al. A history of mild shocks experienced by the regolith particles on hydrated asteroid Ryugu. *Nat. Astron* 7, 669-677 (2023)
[9] Eisenberg, D. and Kauzmann, W. The structure and properties of water, New-York: Oxford University Press, 296 pp. (1969)
[10] Bishop, J. L. et al. Infrared spectroscopic analyses on the nature of water in montmorillonite, *Clays Clay Miner.* 42, N°6, 702-716 (1994)
[11] Ojha, D. et al. On the Hydrogen Bond Strength and Vibrational Spectroscopy of Liquid Water. *Sci. Rep.* 8, 16888 (2018)
[12] Le Pivert-Jolivet, T. et al. Space weathering and pristineness of Ryugu samples from MicrOmega spectral analyses. *Nat. Astron.* 7, 1445-1453 (2023)
[13] Lane, M. D. et al., Spectra of Phosphate Minerals as Obtained by Visible-Near Infrared Reflectance, Thermal Infrared Emission, and Mössbauer Laboratory Analyses, 38th Lunar and Planetary Science Conference, (Lunar and Planetary Science XXXVIII), held March 12-16, 2007 in League City, Texas. LPI Contribution No. 1338, p.2210
[14] Jastrzebski, W., et al. Infrared spectroscopy of different phosphates structures. *Spectrochim. Acta A* 79, 722– 727 (2011)
[15] Banks, E. et al. Chemistry of Struvite Analogs of the Type MgMP04-6H20 (M+ = K+ Rb+ Cs+, T1+, NH4+). *Inorg. Chem.* 14, No. 7 (1975)
[16] Bishop, J. L. et al. Detection of soluble and fixed NH 4+ in clay minerals by DTA and IR reflectance spectroscopy: a potential tool for planetary surface exploration*. Planet. Space Sci.* 50, Issue 1, p. 11-19 (2002)
[17] Berg, B., L. Reflectance spectroscopy (0.35-8 µm) of ammonium-bearing minerals and qualitative comparison to Ceres-like asteroids. *Icarus* 265, p. 218-237 (2016)
[18] Krohn, M.D. and Altaner, S. P. Near-infrared detection of ammonium minerals. *Geophysics* 52, N°7 (1987)
[19] Ehlmann, B. L., et al. Ambient and cold-temperature infrared spectra and XRD patterns of ammoniated phyllosilicates and carbonaceous chondrite meteorites relevant to Ceres and other solar system bodies. *Meteorit. Planet. Sci.* 53, Issue 9, pp. 1884-1901 (2018)
[20] Fastelli, M., et al. Reflectance spectra (1-5 µm) at low temperatures and different grain sizes of ammonium-bearing minerals relevant for icy bodies. *Icarus* 382, article id. 115055 (2022)
[21] Chiari and Ferraris. The water molecule in crystalline hydrates studied by neutron diffraction. *Acta Cryst.* B38, 2331-2341 (1982)
[22] Zhang, A.-C. et al. Young asteroidal fluid activity revealed by absolute age from apatite in carbonaceous chondrite. *Nat. Commun.* 7, 12844 (2016)
[23] Piralla, M. et al. Apatite halogen and hydrogen isotope constraints on the conditions of hydrothermal alteration in carbonaceous chondrites. *Meteorit. Planet. Sci.* 56, Issue 4, pp. 809-828 (2011)
[24] Ma, C. et al. Mg-Phosphate from Asteroid Ryugu: An Original H_2O-Rich Phase, 85th Annual Meeting of The Meteoritical Society, held August 14-19, 2022 in Glasgow, Scotland. LPI Contribution No. 2695, id.6134
[25] Lee, M. R. and Nicholson, K. Ca-carbonate in the Orgueil (CI) carbonaceous chondrite: mineralogy, microstructure and implications for parent body history. *Earth Planet. Sci. Lett.* 280, 268-275 (2009)

500 [26] Hopp, T. et al. Ryugu's nucleosynthetic heritage from the outskirts of the Solar System. *Sci. Adv.*
501 8, issue 46, id. eadd8141 (2022)
502 [27] Kawasaki, N. Oxygen isotopes of anhydrous primary minerals show kinship between asteroid
503 Ryugu and comet 81P/Wild2. *Sci. Adv.* 8, issue 50, id. eade2067 (2022)
504 [28] Nakashima, D. et al. Chondrule-like objects and Ca-Al-rich inclusions in Ryugu may potentially be
505 the oldest Solar System materials. *Nat. Commun.* 14, article id. 532 (2023)
506 [29] McClure, M. K. et al. An Ice Age JWST inventory of dense molecular cloud ices. *Nat. Astron.* 7,
507 431-443 (2023)
508 [30] Poch, O. et al. Ammonium salts are a reservoir of nitrogen on a cometary nucleus and possibly
509 on some asteroids. *Science* 367, Issue 6483, id. aaw7462 (2020).
510 [31] Yokoyama, T. et al. Samples returned from the asteroid Ryugu are similar to Ivuna-type
511 carbonaceous meteorites. *Science* 379, Issue 6634, article id. abn7850 (2023)
512 [32] Verchovsky, A. B. et al. Ryugu's volatiles investigated using stepped combustion and EGA
513 methods. 54th Lunar and Planetary Science Conference, 2023, abstract #2806.
514 [33] McCain, K. A. et al. Early fluid activity on Ryugu inferred by isotopic analyses of carbonates and
515 magnetite. *Nat. Astron.* 7, 309-317 (2023)
516 [34] Gull, M. and Pasek, M. Is Struvite a Prebiotic Mineral? *Life* 3, issue 2, 321-330 (2013)
517 [35] Reddy, M. M. Crystallization of calcium carbonate in the presence of trace concentrations of
518 phosphorus-containing anions. *J. Cryst. Growth* 41, 287-295 (1977)
519 [36] House, W. A. Inhibition of calcite crystal growth by inorganic phosphate. *J. Colloid Interface Sci.*
520 119 (1987)
521 [37] Cao, X. and Harris, W. Carbonate and magnesium interactive effect on calcium phosphate
522 precipitation. *Environ. Sci. Technol*. 42, 436-442 (2008)
523 [38] Toner, J. D. and Catling D. C. A carbonate-rich lake solution to the phosphate problem of the
524 origin of life. *PNAS* 117, 883-888 (2020)
525 [39] Brunetto, R. et al. Ryugu's Anhydrous Ingredients and Their Spectral Link to Primitive Dust from
526 the Outer Solar System. *Ap J. L.* 951, Issue 2, id.L33, 8 pp. (2023)
527 [40] Feng, T. et al. Evolution of ephemeral phosphate minerals on planetary environments*. ACS Earth*
528 *Space Chem.* 5, 1647-1656 (2021)
529 [41] Yabuta, H. et al. Macromolecular organic matter in samples of the asteroid (162173) Ryugu.
530 *Science* 379, Issue 6634, article id. abn9057 (2023)
531 [42] Naraoka, H. et al. Soluble organic molecules in samples of the carbonaceous asteroid (162173)
532 Ryugu. *Science* 379, Issue 6634, article id. abn9033 (2023)
533 [43] Oba, Y., et al. Uracil in the carbonaceous asteroid (162173) Ryugu. *Nat. Commun.* 14, article id.
534 129 (2023)
535 [44] Walton, C. R. et al. Cosmic dust fertilization of glacial prebiotic chemistry on early Earth. *Nat.*
536 *Astron.* Advanced Online Publication (2024)
537 [45] Gulick, A. Phosphorus as a factor in the origin of life. *Am. Sci.* 43, 479–489 (1955)
538 [46] Walton, C. R. et al. Phosphorus availability on the early Earth and the impacts of life. *Nat. Geosci.*
539 16, 399-409 (2023)
540 [47] Handschuh, G. J. et al. The effect of Mg2+ and Ca2+ on urea-catalyzed phosphorylation
541 reactions*. J. of Mol. Evol.* 2, issue 4, pp. 251-262 (1973)
542 [48] Orgel, L.E. and Lohrmann, R. Prebiotic Chemistry and Nucleic Acid Replication. *Acc. Chem. Res.* 7,
543 11, 368–377 (1974)
544 [49] Redfield, A. C. The Biological Control of Chemical Factors in the Environment. *Am. Sci.* 46, n^{o} 3,
545 205–221, 230A (1958)
546 [50] Pasek, M. A. et al. Phosphorylation on the early earth. *Chem. Geol.* 475, 149-170 (2017)
547 [51] Handschuh, G. J. and Orgel, L. E. Struvite and Prebiotic Phosphorylation. *Science* 179, Issue 4072,
548 pp. 483-484 (1973)
549 [52] Osterberg, R. and Orgel, L.E. Polyphosphate and trimetaphosphate formation under potentially
550 prebiotic conditions. *J. Mol. Evol.* 1, issue 3, pp. 241-248 (1972)
551 [53] Gull, M. Prebiotic Phosphorylation Reactions on the Early Earth. *Challenges* 5, 193-212 (2014)

[54] Burcar, B. et al. Darwin's Warm Little Pond: A One-Pot Reaction for Prebiotic Phosphorylation and the Mobilization of Phosphate from Minerals in a Urea-Based Solvent. *Angew. Chem.* 128, issue 42, pp. 13443-13447 (2016)
[55] Riu, L. et al. Calibration and performances of the MicrOmega instrument for the characterization of asteroid Ryugu returned samples. *Rev. Sci. Instrum.* 93, 054503 (2022)
[56] Li, X. et al. GaN Schottky barrier diodes with nickel nitride anodes sputtered at different nitrogen partial pressure. *Vacuum* 162, 72-77 (2019)
[57] Starkey, N. A. and Franchi, I. A. Insight into the silicate and organic reservoirs of the comet forming region. *Geochim. Cosmochim. Acta* 105, 73-91 (2013)
[58] Lodders, K. Relative Atomic Solar System Abundances, Mass Fractions, and Atomic Masses of the Elements and Their Isotopes, Composition of the Solar Photosphere, and Compositions of the Major Chondritic Meteorite Groups. *Space Sci. Rev.* 217, Issue 3, article id.44 (2021)
[59] Bayuseno, A. P. and Schmahl, W. W. Crystallization of struvite in a hydrothermal solution with and without calcium and carbonate ions. *Chemosphere* 250, 126245 (2020)
[60] Benezeth, P., et al. Solubility product of siderite (FeCO3) as a function of temperature (25–250 °C). *Chem. Geol.* 265, 3-12 (2009)
[61] Benezeth, P., et al. Experimental determination of the solubility product of magnesite at 50 to 200 °C. *Chem. Geol.* 286, 21-31 (2011)

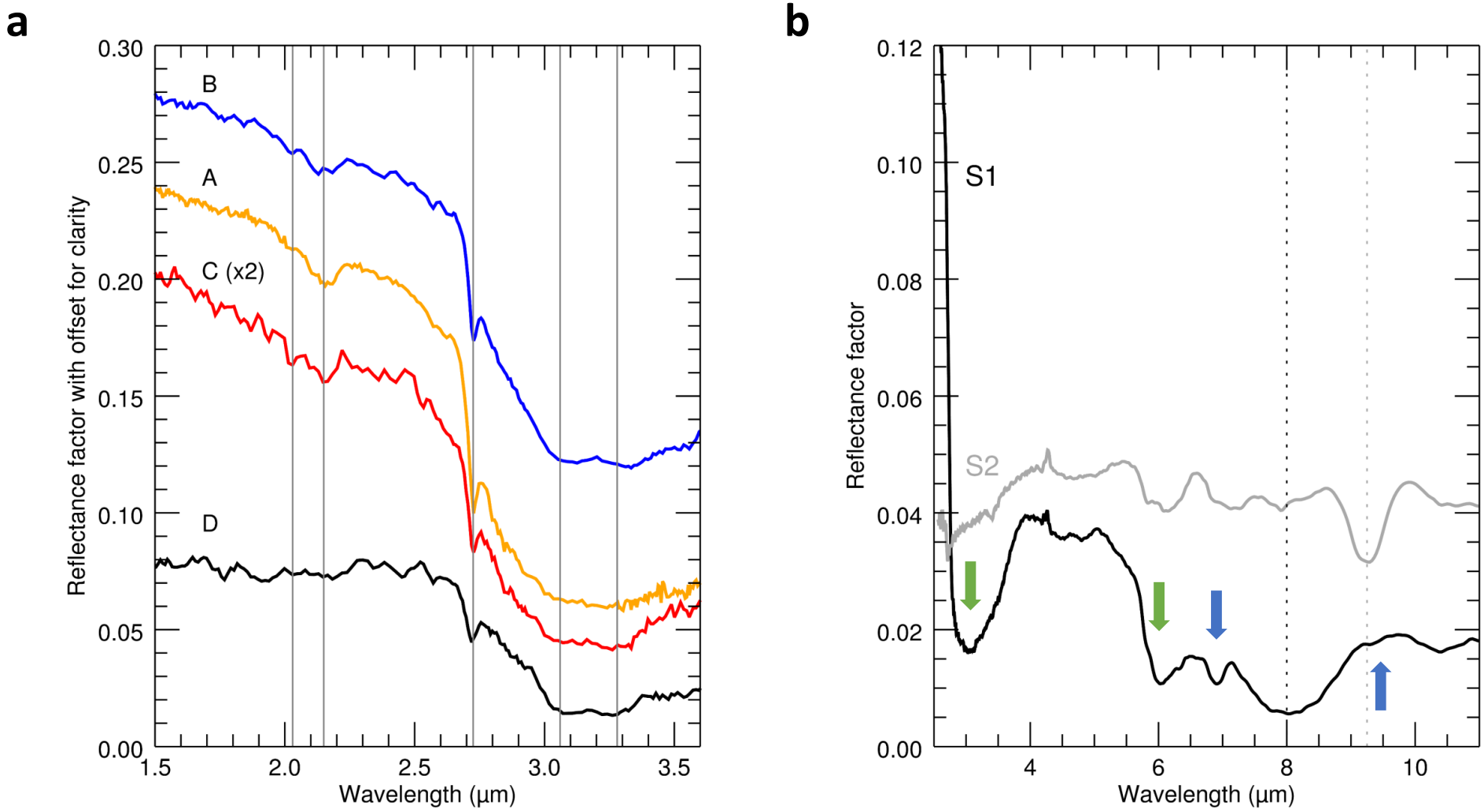
a
b
B
A
C (x2)
D
S1
S2
Reflectance factor with offset for clarity
Reflectance factor
Wavelength (μm)
Wavelength (μm)
0.30
0.25
0.20
0.15
0.10
0.05
0.00
0.12
0.10
0.08
0.06
0.04
0.02
0.00
1.5
2.0
2.5
3.0
3.5
4
6
8
10

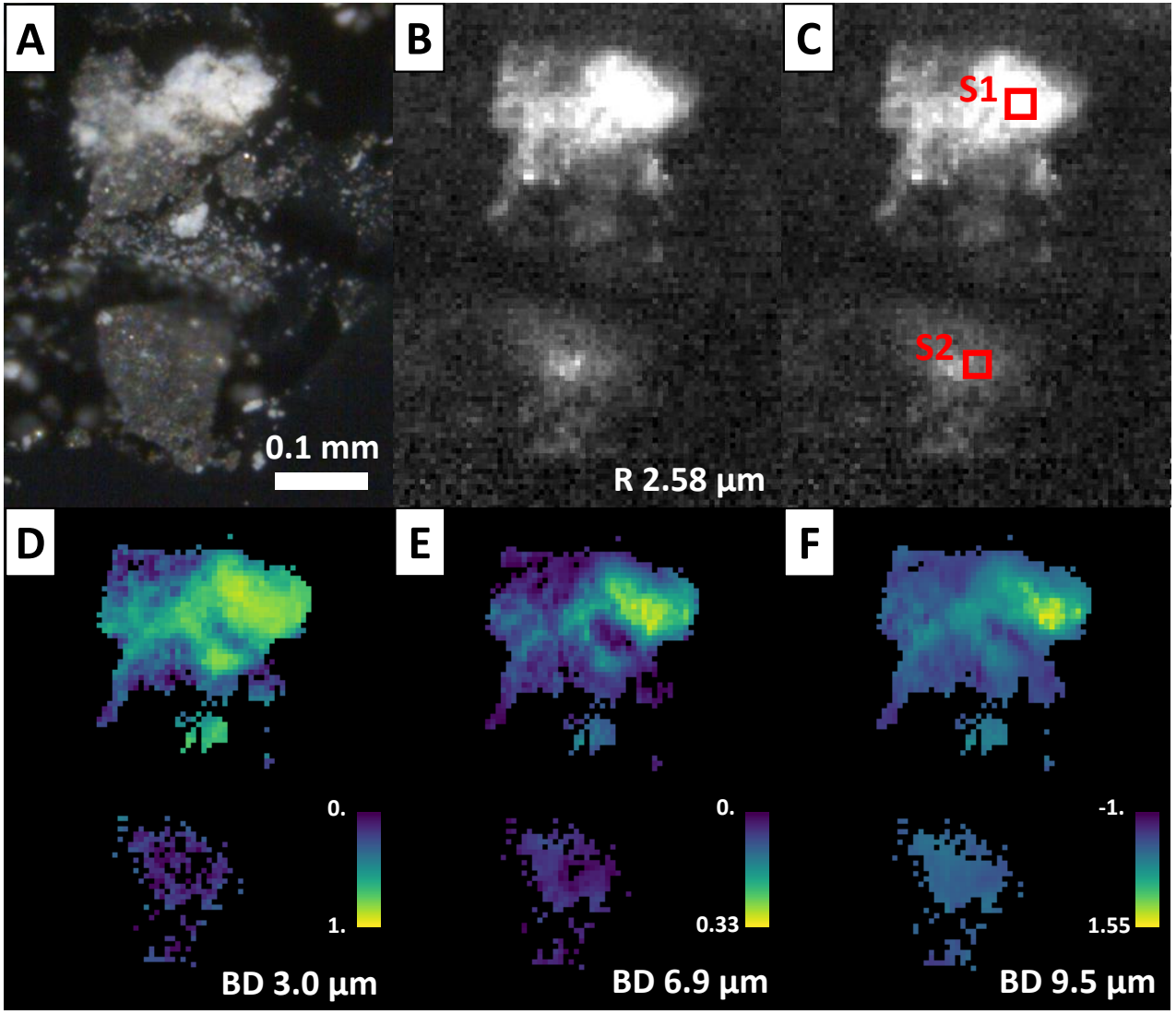
A
B
C
S1
S2
0.1 mm
R 2.58 µm
D
E
F
0.
1.
0.
0.33
-1.
1.55
BD 3.0 µm
BD 6.9 µm
BD 9.5 µm

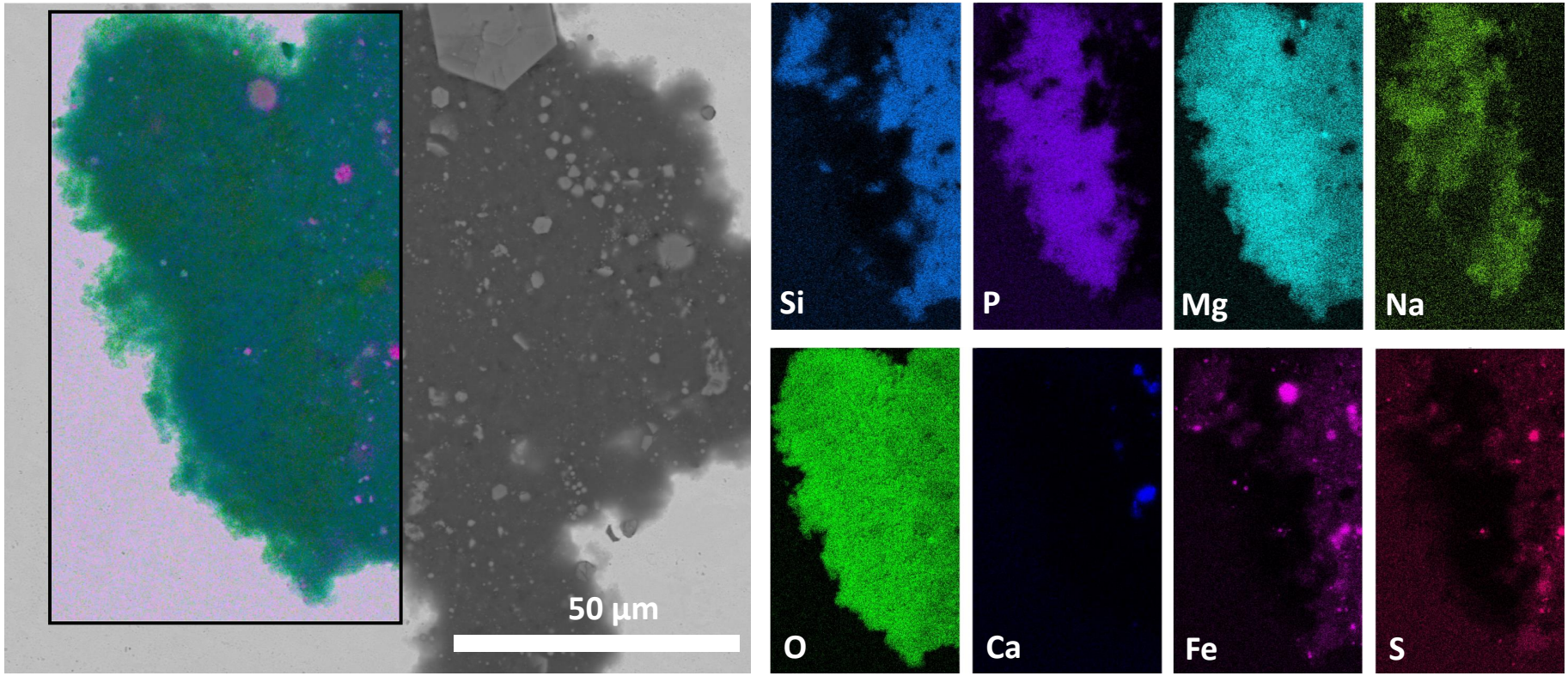
50 µm
Si
P
Mg
Na
O
Ca
Fe
S

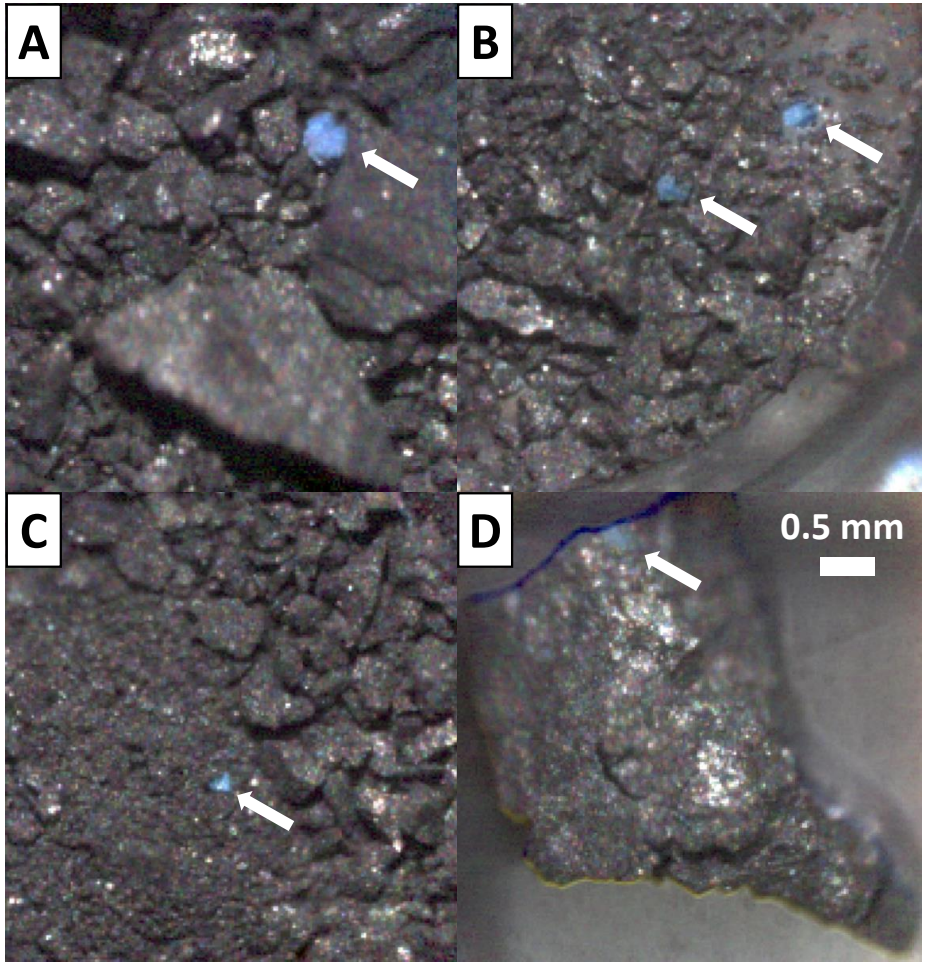
A
B
C
D
0.5 mm

C0209	Na_2O	MgO	Al_2O_3	SiO_2	P_2O_5	SO_3	K_2O	CaO	Cr_2O_3	FeO	Normalized to 100wt%
C0209,0,2.21											
Point#1	2.02	27.15	2.05	30.15	14.01	9.00	0.14	0.27	0.61	14.60	100
Point#2	1.04	33.52	0.30	2.80	52.24	0.72	B.D.	0.16	0.00	9.22	100
Point#3	2.60	23.29	0.98	24.23	15.29	9.35	0.14	0.74	0.73	22.64	100
Point#4	2.47	24.33	1.88	32.66	4.67	11.80	B.D.	0.29	0.36	21.54	100
Point#6	0.13	34.33	0.62	0.91	59.73	0.50	0.07	0.07	B.D.	3.65	100
Point#7	0.63	20.95	2.25	30.80	2.25	17.12	0.14	0.27	0.78	24.81	100
Point#8	2.33	29.83	0.67	13.37	38.16	5.55	0.18	0.39	0.21	9.30	100
C0209,0,2,22											
Point#9	1.38	23.82	2.58	35.99	0.79	10.12	B.D.	0.03	0.95	24.35	100
Point#10	1.72	14.24	0.86	19.28	2.50	12.83	B.D.	0.31	1.62	46.64	100
Point#11	1.38	13.42	1.87	6.86	5.53	2.70	0.09	0.36	0.00	67.79	100

A0218	Na_2O	MgO	Al_2O_3	SiO_2	P_2O_5	SO_3	K_2O	CaO	Cr_2O_3	FeO	Normalized to 100wt%
Point#11	0.01	36.70	B.D.	0.30	62.81	B.D.	0.07	0.01	B.D.	0.09	100
Point#12	0.03	34.45	B.D.	0.41	64.56	0.14	0.07	0.04	0.02	0.28	100
Point#13	0.05	28.26	0.05	0.65	70.11	B.D.	0.06	0.02	0.10	0.71	100
Point#14	0.10	34.86	0.10	0.45	64.10	B.D.	B.D.	0.07	B.D.	0.32	100
Point#15	0.09	31.65	0.02	0.85	66.56	0.21	0.05	0.00	0.04	0.53	100
Point#16	3.12	25.47	2.26	37.98	0.05	14.57	0.14	0.31	0.53	15.56	100
Point#17	1.11	11.07	1.20	27.30	B.D.	10.10	0.21	0.00	1.68	47.33	100
Point#18	0.40	4.66	0.74	15.05	0.06	12.26	0.04	0.02	2.63	64.15	100
Point#19	2.84	24.03	2.41	38.11	0.15	14.85	0.11	0.02	0.37	17.09	100
Point#20	4.61	22.75	2.36	40.52	B.D.	11.64	0.31	0.07	0.67	17.08	100
Point#21	54.13	6.75	0.74	9.90	0.81	17.62	0.24	3.62	0.33	5.85	100

B.D.: below detection limit

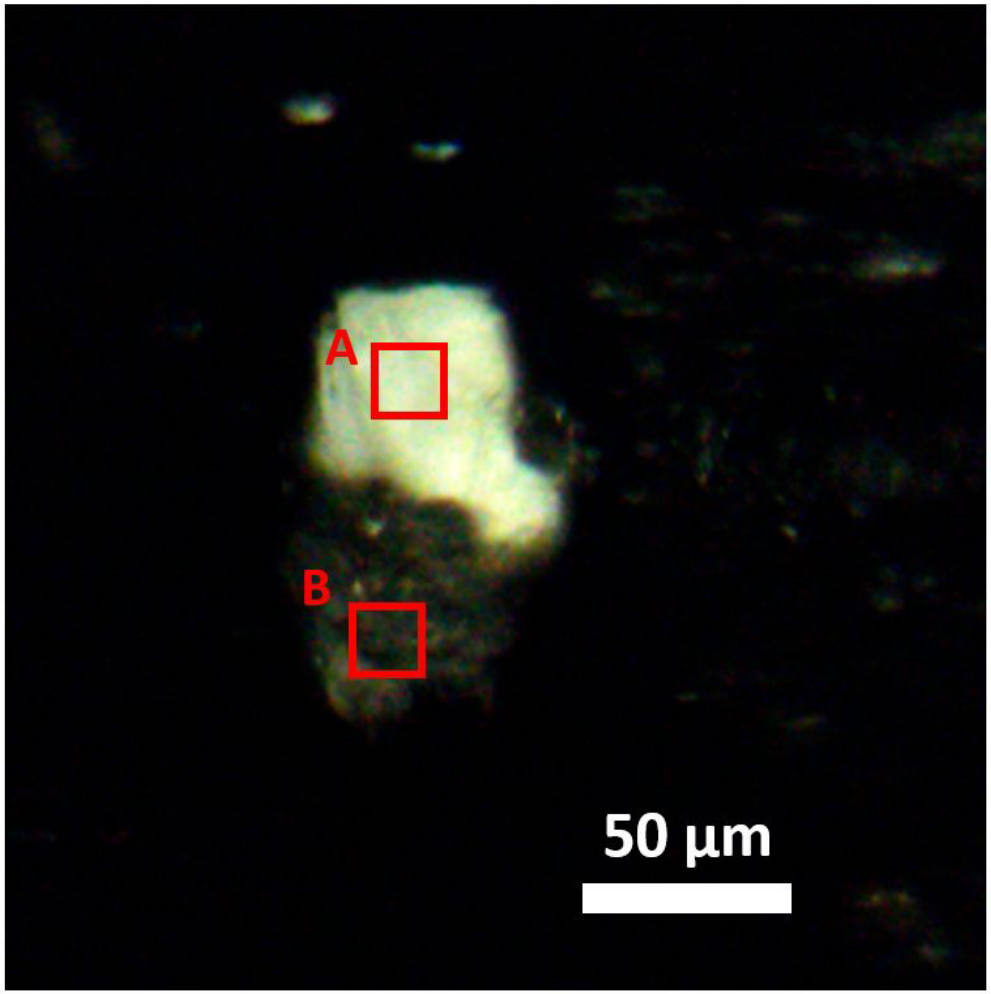
A
B
50 µm

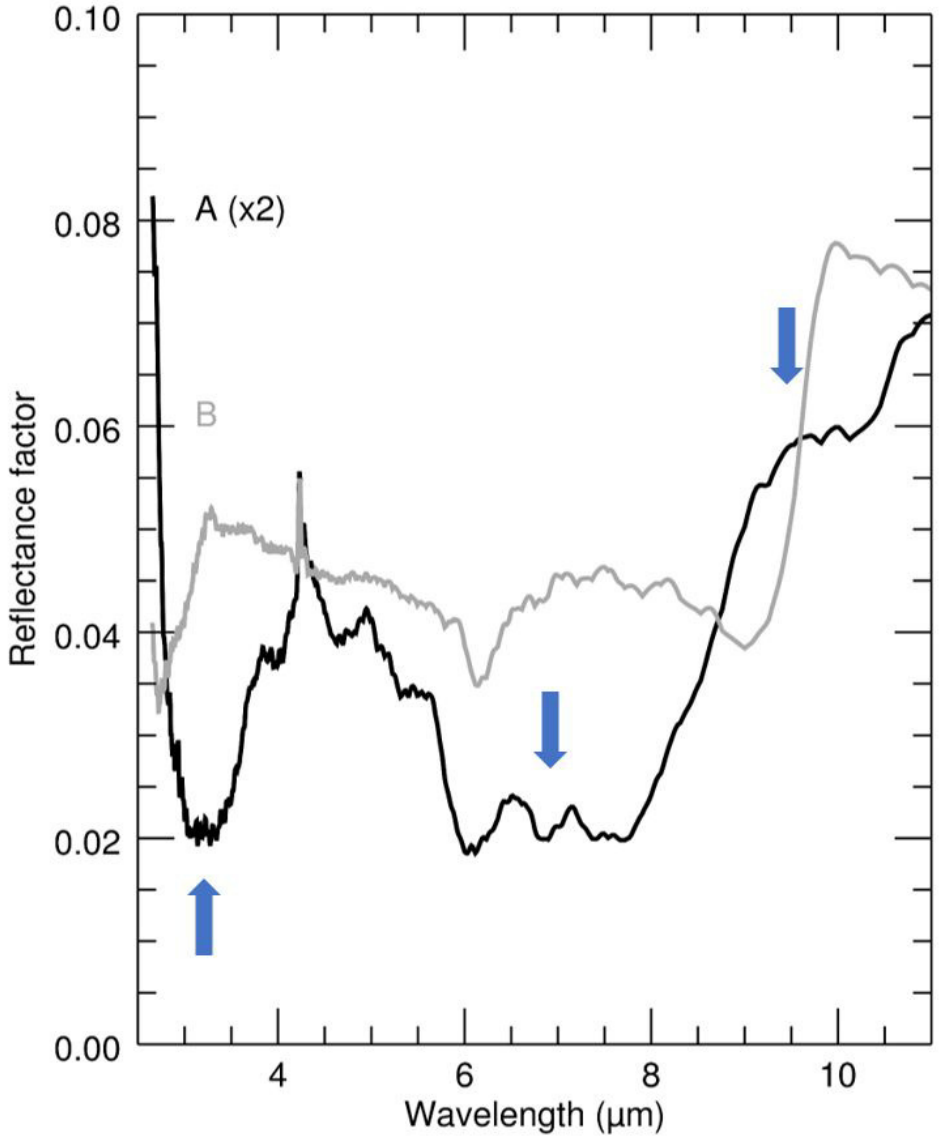
0.10
0.08
0.06
0.04
0.02
0.00
Reflectance factor
A (x2)
B
4
6
8
10
Wavelength (µm)

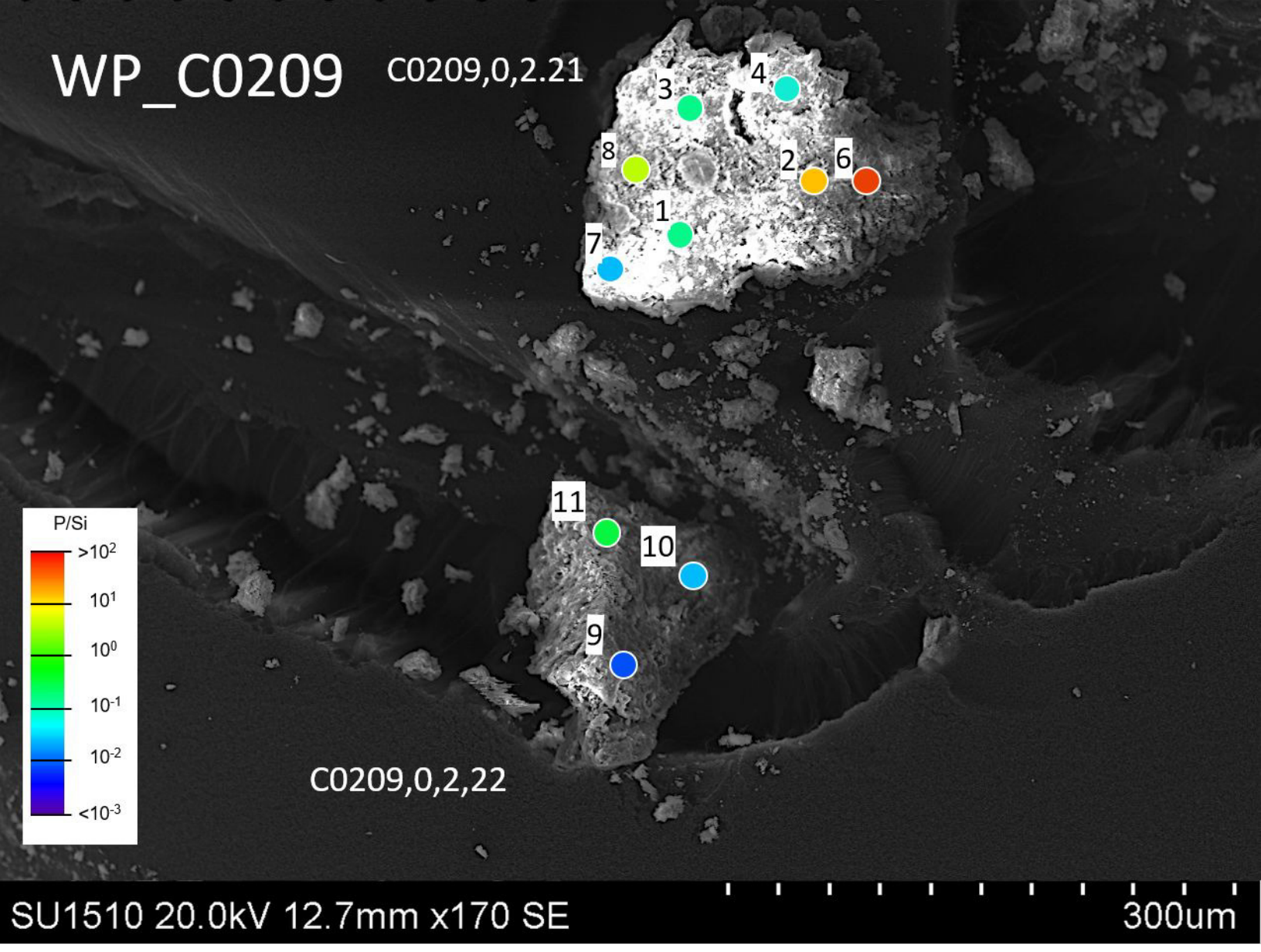
WP_C0209
C0209,0,2.21
3
4
8
2
6
1
7
11
10
9
P/Si
>10^2
10^1
10^0
10^-1
10^-2
<10^-3
C0209,0,2,22
SU1510 20.0kV 12.7mm x170 SE
300um

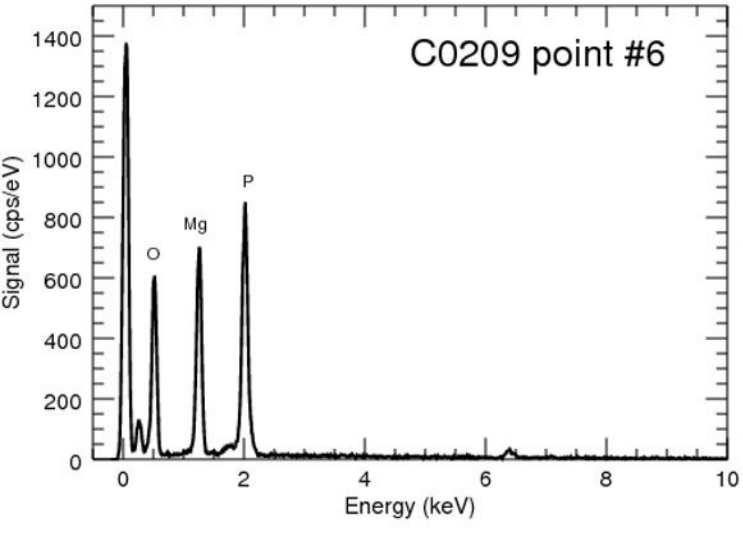
C0209 point #6
Signal (cps/eV)
Energy (keV)
O
Mg
P

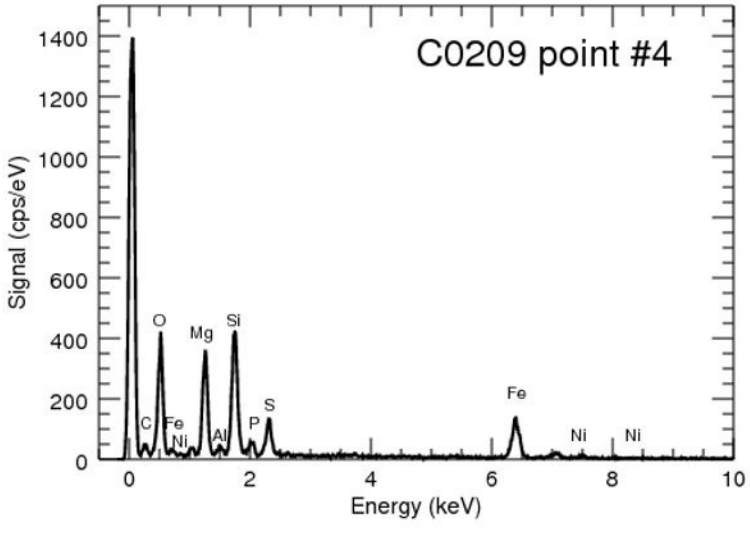
C0209 point #4
Signal (cps/eV)
Energy (keV)
C
O
Fe
Ni
Mg
Al
Si
P
S
Fe
Ni
Ni

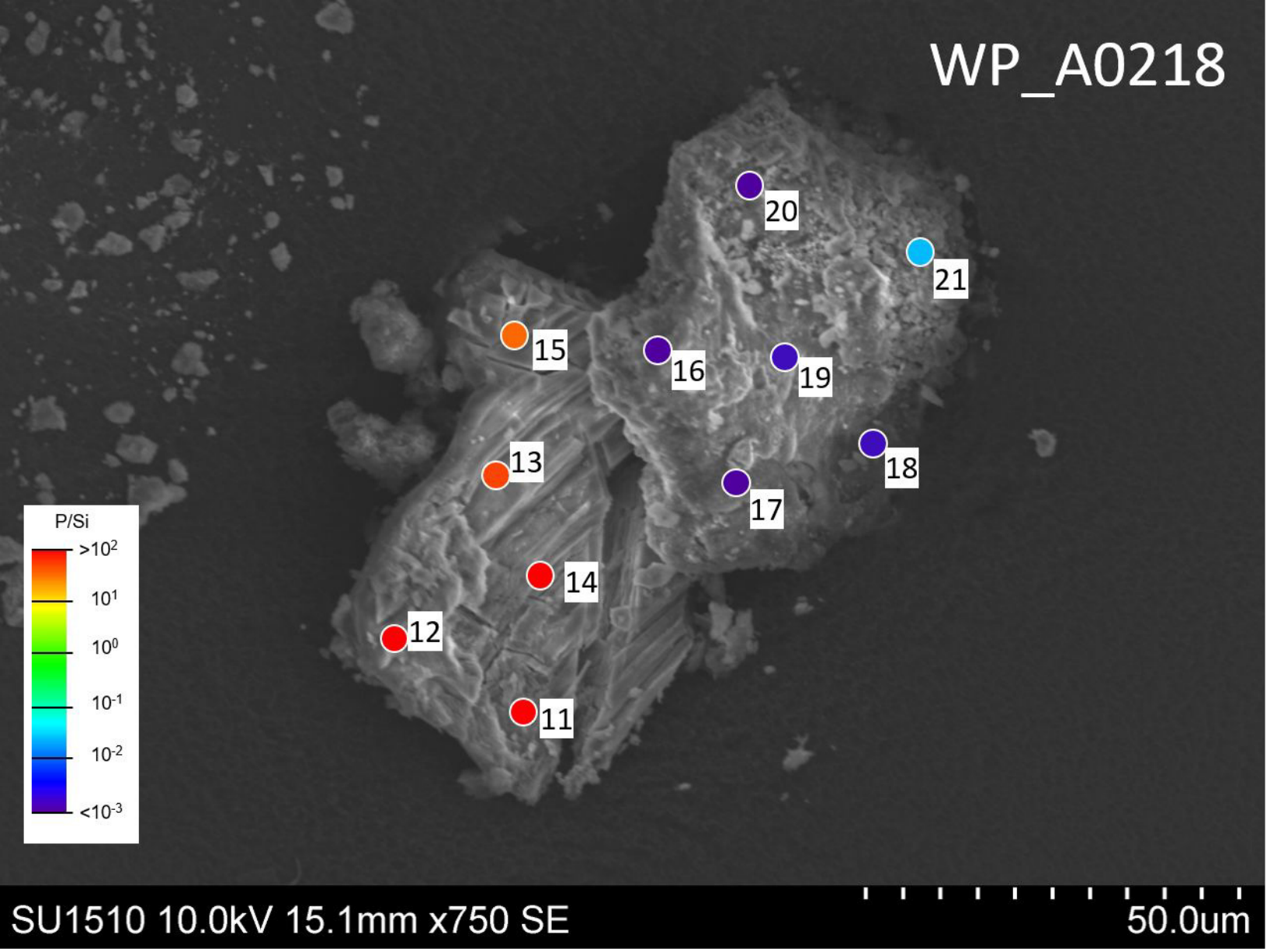
WP_A0218
20
21
15
16
19
18
13
17
14
12
11
P/Si
>10^2
10^1
10^0
10^-1
10^-2
<10^-3
SU1510 10.0kV 15.1mm x750 SE
50.0um

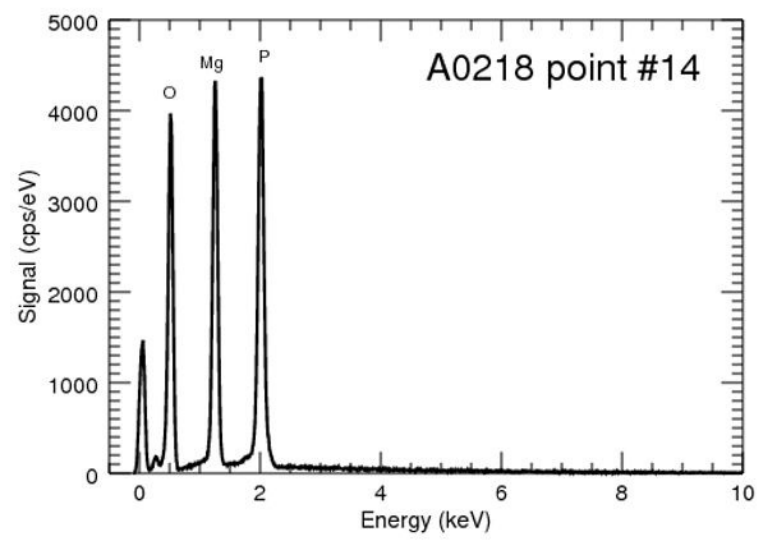
A0218 point #14
O
Mg
P
Signal (cps/eV)
Energy (keV)
0
1000
2000
3000
4000
5000
0
2
4
6
8
10

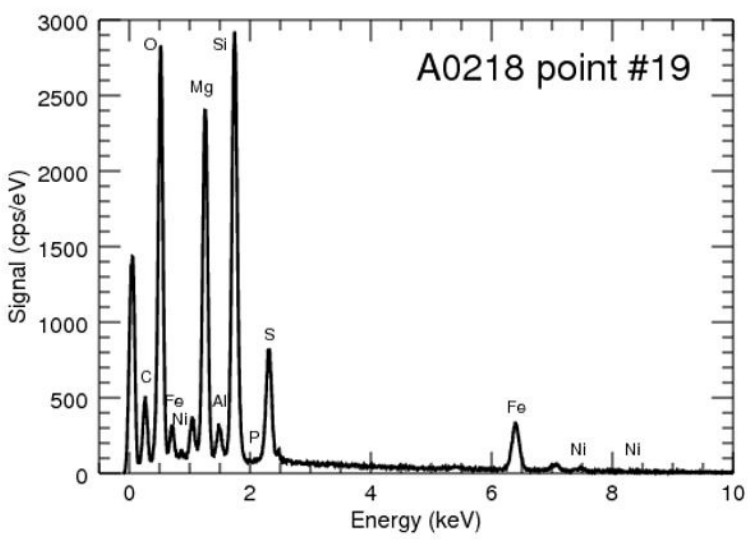
A0218 point #19
O
Si
Mg
C
Fe
Ni
Al
P
S
Fe
Ni
Ni
Signal (cps/eV)
Energy (keV)
0
500
1000
1500
2000
2500
3000
0
2
4
6
8
10

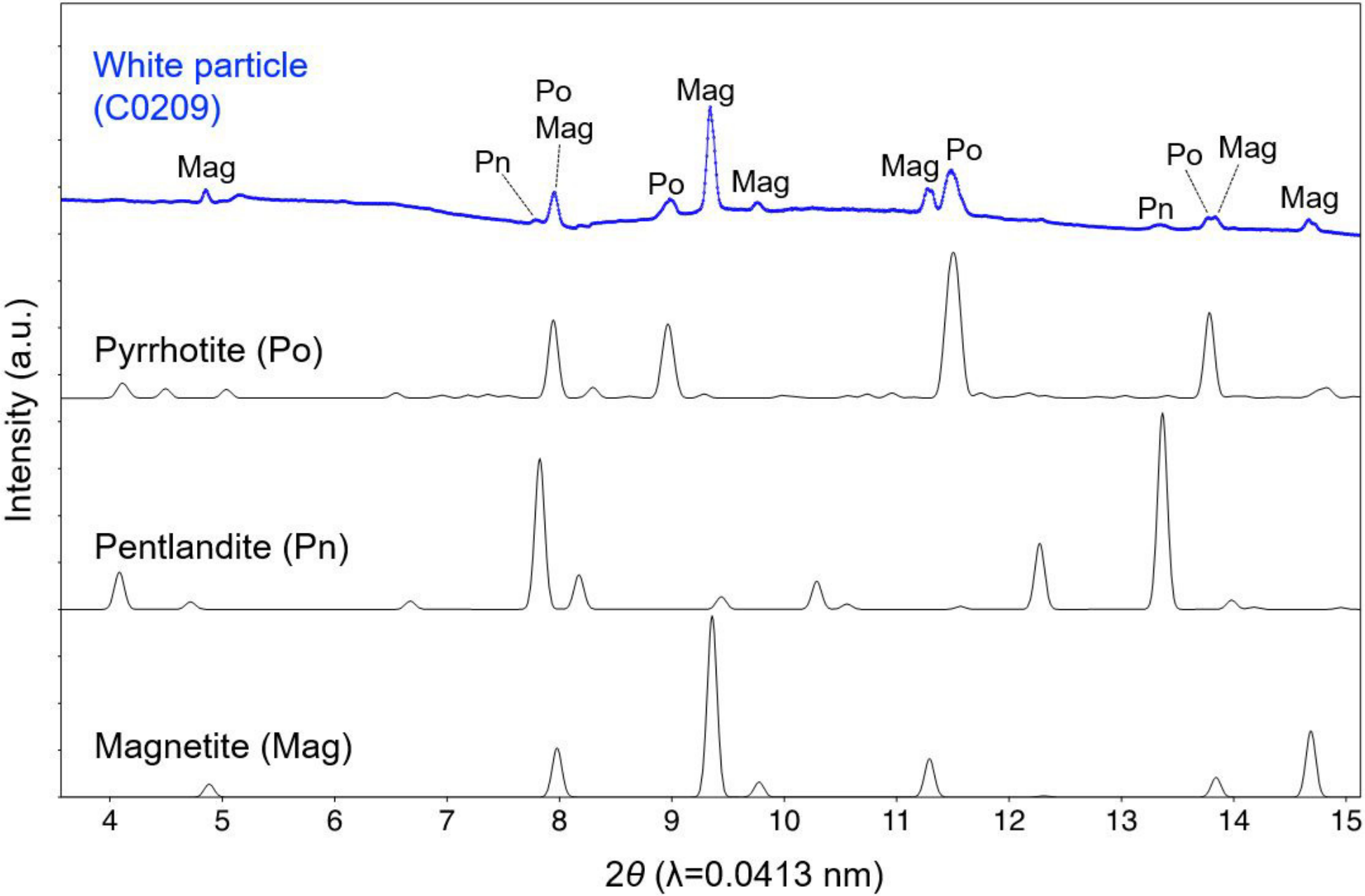
White particle
(C0209)
Mag
Pn
Po
Mag
Po
Mag
Mag
Mag
Po
Pn
Po
Mag
Mag
Pyrrhotite (Po)
Pentlandite (Pn)
Magnetite (Mag)
Intensity (a.u.)
4
5
6
7
8
9
10
11
12
13
14
15
2θ (λ=0.0413 nm)

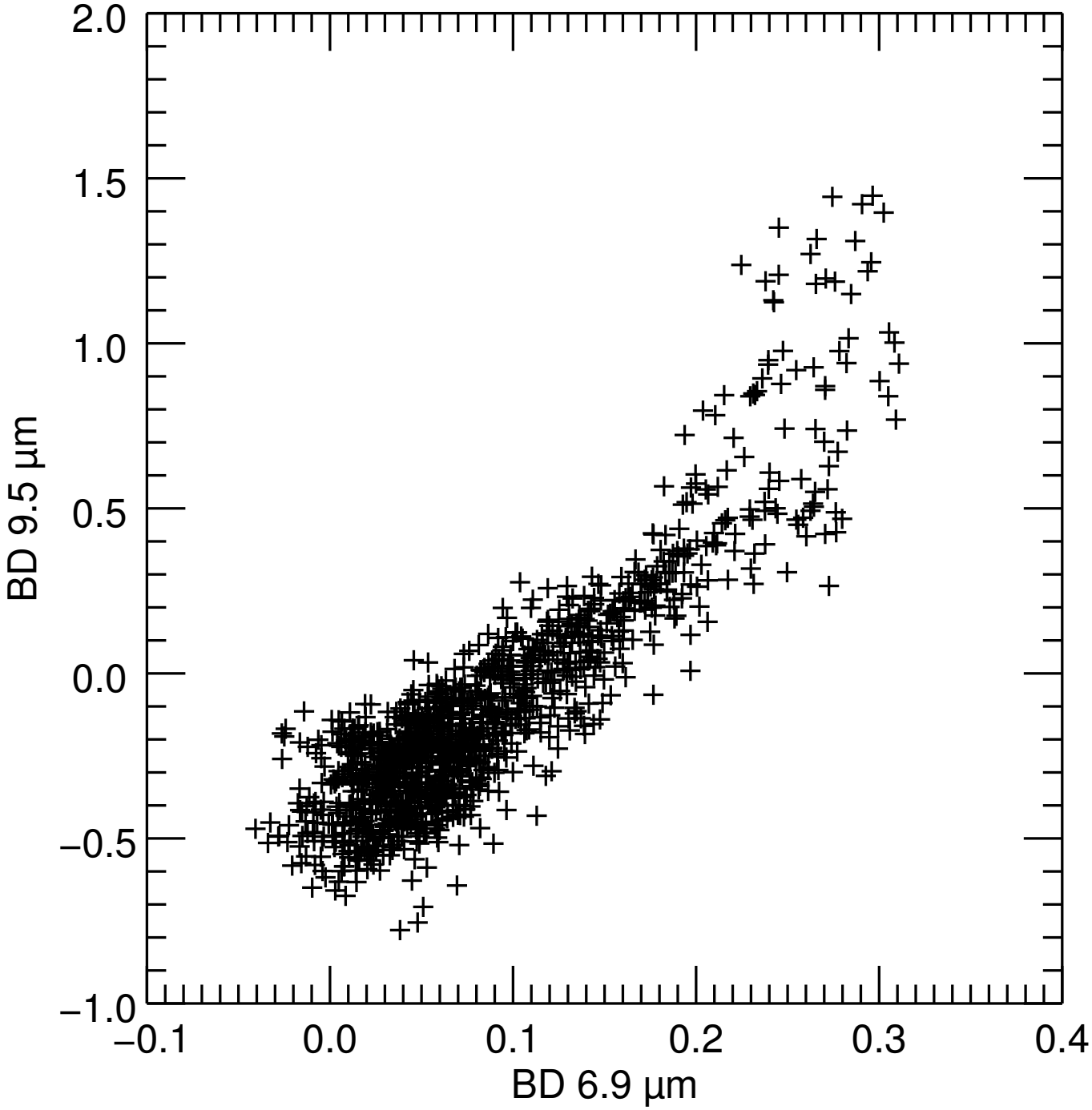
2.0
1.5
1.0
0.5
0.0
−0.5
−1.0
BD 9.5 µm
−0.1
0.0
0.1
0.2
0.3
0.4
BD 6.9 µm

C0209	Na/Mg	Al/Mg	Si/Mg	P/Mg	S/Mg	K/Mg	Ca/Mg	Cr/Mg	Fe/Mg	P/Si
Point#1	0,0968	0,0597	0,7449	0,293	0,1669	0,0044	0,0071	0,0119	0,3017	0,3934
Point#2	0,0404	0,0071	0,056	0,885	0,0108	0	0,0034	0	0,1543	15,7948
Point#3	0,1452	0,0333	0,6979	0,3728	0,2021	0,0051	0,0228	0,0166	0,5454	0,5342
Point#4	0,132	0,0611	0,9005	0,109	0,2442	0	0,0086	0,0078	0,4967	0,1211
Point#6	0,0049	0,0143	0,0178	0,9881	0,0073	0,0017	0,0015	0	0,0596	55,5672
Point#7	0,0391	0,0849	0,9862	0,061	0,4114	0,0057	0,0093	0,0197	0,6644	0,0618
Point#8	0,1016	0,0178	0,3007	0,7265	0,0937	0,0052	0,0094	0,0037	0,1749	2,4163
Point#9	0,0753	0,0856	1,0135	0,0188	0,2139	0	0,0009	0,0212	0,5735	0,0186
Point#10	0,1571	0,0477	0,9082	0,0997	0,4536	0	0,0156	0,0603	1,8375	0,1098
Point#11	0,1337	0,1102	0,3429	0,234	0,1013	0,0057	0,0193	0	2,834	0,6824

A0218	Na/Mg	Al/Mg	Si/Mg	P/Mg	S/Mg	K/Mg	Ca/Mg	Cr/Mg	Fe/Mg	P/Si
Point#11	0,0004	0	0,0055	0,9719	0	0,0016	0,0002	0	0,0014	177,2455
Point#12	0,0011	0	0,008	1,0642	0,002	0,0017	0,0008	0,0003	0,0046	133,3053
Point#13	0,0023	0,0014	0,0154	1,4089	0	0,0018	0,0005	0,0019	0,0141	91,3133
Point#14	0,0037	0,0023	0,0087	1,0442	0	0	0,0014	0	0,0052	120,5905
Point#15	0,0037	0,0005	0,018	1,1943	0,0033	0,0014	0	0,0007	0,0094	66,2921
Point#16	0,1593	0,0702	1,0003	0,0011	0,288	0,0047	0,0087	0,011	0,3427	0,0011
Point#17	0,1304	0,0857	1,6543	0	0,4593	0,0162	0	0,0805	2,3987	0
Point#18	0,1116	0,1255	2,1664	0,0073	1,3244	0,0073	0,0031	0,2993	7,7232	0,0034
Point#19	0,1537	0,0793	1,0639	0,0035	0,3111	0,0039	0,0006	0,0082	0,399	0,0033
Point#20	0,2635	0,082	1,1948	0	0,2576	0,0117	0,0022	0,0156	0,4212	0
Point#21	10,4296	0,0867	0,9838	0,0681	1,3141	0,0304	0,3855	0,0259	0,4862	0,0693

Mineral formula	Name	pKs (at 298K)	Ref.	Calculated solubility in mol/L (at 298K)	Deduced phosphate ion concentration at equilibrium in mol/L (at 298 K)
$Ca_5(PO_4)_3(OH)$	hydroxyapatite	54.45	[59]	2.53×10^{-7}	7.58×10^{-7}
$CaMg(CO_3)_2$	dolomite	17.09	[59]	3.78×10^{-5}	---
$NH_4MgPO_4 \cdot 6H_2O$	struvite	13.17	[59] and references therein	4.07×10^{-5}	4.07×10^{-5}
$FeCO_3$	siderite	10.90	[60]	3.55×10^{-6}	---
$CaCO_3$	calcite	8.48	[59]	5.75×10^{-5}	---
$CaCO_3$	aragonite	8.34	[59]	6.76×10^{-5}	---
$MgCO_3$	magnesite	7.80	[61]	1.26×10^{-4}	---

Atomic number	Element	E/Si in CIs (calculated from [58])	E/Si uncertainty (calculated from [58])	E/Si in Ryugu samples (calculated from XRF analyses in [31])	E/Si uncertainty (calculated from XRF analyses in [31])
6	C	0.8937	0.2415	0.8248	0.0177
8	O	7.3679	0.8171	5.3134	0.0667
11	Na	0.0576	0.0095	0.0741	0.0018
12	Mg	1.0303	0.1122	1.1478	0.0120
13	Al	0.0806	0.0112	0.0824	0.0014
14	Si	1.0000	0.1337	1.0000	
15	P	0.0082	0.0016	0.0073	0.0001
16	S	0.4353	0.0648	0.3355	0.0040
17	Cl	0.0053	0.0024	0.0048	0.0002
19	K	0.0036	0.0006	0.0032	0.0001
20	Ca	0.0574	0.0084	0.0780	0.0014
22	Ti	0.0024	0.0003	0.0022	0.0002
24	Cr	0.0130	0.0019	0.0143	0.0004
25	Mn	0.0090	0.0014	0.0101	0.0003
26	Fe	0.8617	0.1179	0.7220	0.0092
27	Co	0.0022	0.0003	0.0022	0.0001
28	Ni	0.0484	0.0063	0.0420	0.0004